



This open access document is posted as a preprint in the Beilstein Archives at <https://doi.org/10.3762/bxiv.2020.136.v1> and is considered to be an early communication for feedback before peer review. Before citing this document, please check if a final, peer-reviewed version has been published.

This document is not formatted, has not undergone copyediting or typesetting, and may contain errors, unsubstantiated scientific claims or preliminary data.

Preprint Title Imaging of SARS-CoV-2 infected Vero E6 Cells by Helium Ion Microscopy

Authors Natalie Frese, Patrick Schmerer, Martin Wortmann, Matthias Schürmann, Matthias König, Michael Westphal, Friedemann Weber, Holger Sudhoff and Armin Götzhäuser

Publication Date 03 Dec 2020

Article Type Full Research Paper

ORCID® iDs Martin Wortmann - <https://orcid.org/0000-0002-5101-4643>; Matthias König - <https://orcid.org/0000-0001-5877-6643>; Friedemann Weber - <https://orcid.org/0000-0001-9737-337X>; Holger Sudhoff - <https://orcid.org/0000-0002-9274-5645>; Armin Götzhäuser - <https://orcid.org/0000-0002-0838-9028>

License and Terms: This document is copyright 2020 the Author(s); licensee Beilstein-Institut.

This is an open access work under the terms of the Creative Commons Attribution License (<https://creativecommons.org/licenses/by/4.0>). Please note that the reuse, redistribution and reproduction in particular requires that the author(s) and source are credited and that individual graphics may be subject to special legal provisions.

The license is subject to the Beilstein Archives terms and conditions: <https://www.beilstein-archives.org/xiv/terms>.

The definitive version of this work can be found at <https://doi.org/10.3762/bxiv.2020.136.v1>

Imaging of SARS-CoV-2 infected Vero E6 Cells by Helium Ion Microscopy

Natalie Frese ¹, Patrick Schmerer ², Martin Wortmann ³, Matthias Schürmann ⁴,
Matthias König ², Michael Westphal ¹, Friedemann Weber ², Holger Sudhoff ⁴,
Armin Gölzhäuser ^{1*}

¹ Physics of Supramolecular Systems and Surfaces, Faculty of Physics, Bielefeld University, Bielefeld, Germany

² Institute of Virology, Faculty of Veterinary Medicine, Justus-Liebig-University Giessen, Germany

³ Faculty of Engineering and Mathematics, Bielefeld University of Applied Sciences, Bielefeld, Germany

⁴ University Clinic for Otolaryngology, Head and Neck Surgery, Medical Faculty OWL at Bielefeld University, Germany

* Corresponding author

Abstract

Helium ion microscopy (HIM) offers the opportunity to obtain direct views of biological samples such as cellular structures, virus particles, and microbial interactions. Imaging with the HIM combines sub-nanometer resolution, large depth of field, and high surface sensitivity. Due to its charge compensation capability, the HIM can image insulating biological samples without additional conductive coatings. Here, we present an exploratory HIM study of SARS-CoV-2 infected Vero E6 cells, in which several areas of interactions between cells and virus particles, as well as among virus particles, were imaged. The HIM pictures show the three-dimensional appearance of SARS-CoV-2 and the surface of Vero E6 cells at a multiplicity of infection of approximately 1 with great morphological detail. The absence of a conductive coating allows a distinction between virus particles bound to the cell membrane and virus particles lying on top of the membrane. After prolonged imaging, it was found that ion-induced deposition of hydrocarbons from the vacuum renders the sample sufficiently conductive to allow imaging even without charge compensation. The presented images demonstrate the potential of the HIM in bioimaging, especially for the imaging of interactions between viruses and their host organisms.

Keywords

helium ion microscopy, SARS-CoV-2, Vero E6 cells, charge compensation, bioimaging, cell membrane

Introduction

The last decade of helium ion microscopy (HIM) was characterized by a rapid exploration of its sub-nanometer imaging and ion-beam nanofabrication capabilities in materials science and engineering [1]. Although HIM soon proved to be a promising tool in the life sciences, the examination of biological samples by HIM occurred at a much slower pace. In recent years, it has been used in the field of cell biology for imaging various human and animal cells. These include cartilage- [2], cancer- [3], liver- [4], kidney- [5] and stem-cells [6] as well as fibrin fibers [7]. To visualize viruses and their host organisms, HIM has so far been applied to image T4-phage infected *E. coli* bacteria [8], various phases of the life cycle of the bacterial predator *Bdellovibrio bacteriovorus* [9] and the vesicular structure of ethane-oxidizing archaea [10].

In this work, we use HIM to investigate Vero E6 cells infected with the novel severe acute respiratory syndrome coronavirus 2 (SARS-CoV-2). Several members of the family Coronaviridae have been described in the human population and usually cause mild respiratory disease. SARS-CoV-2 demonstrated a world-wide spread causing a significant global public health emergency [11],[12]. As of November 30th, 2020, more than 63 million cases worldwide have been confirmed with the infection and over 1.4 million infected patients have died [13]. African green monkey kidney Vero E6 cells have been reported to support SARS-CoV-2 replication in culture, while many more cell lines have been reported to be refractory to SARS-CoV-2 infection [14]. Both scanning electron microscopy (SEM) and transmission electron microscopy (TEM) have been used to image SARS-CoV-2 [15],[16],[17],[18],[19]. While TEM achieves unsurpassed resolution and can visualize macromolecular structures like spike glycoproteins or transmembrane proteins [20], SEM provides topographic images of infected cells and virus particles distributed on their surfaces, however, after the

samples have been coated with a conductive layer. Conversely, the HIM delivers a topographic image of the uncoated surface morphology of cells and virus particles, allowing to identify and investigate sites, at which a cell is interacting with the virus. While its principle of operation is very similar to SEM, HIM utilizes a beam of positively charged helium ions (He^+) instead of negatively charged electrons to excite and detect secondary electrons from the sample surface. Due to the high brightness and low energy spread of its atomically sharp gas field ion source, the smallest attainable focused spot size is about 0.3 nm [21]. With its significantly smaller convergence angle compared to SEM, HIM achieves a much larger depth of field, which is particularly useful for imaging three-dimensional structures [21]. Due to their higher mass, the He^+ ions penetrate deeper into the sample and do not spread as wide as electrons, resulting in a smaller escape volume of the secondary electrons and a higher surface resolution of the HIM, compared to the SEM [22]. A further benefit of HIM is its charge compensation capability during secondary electron detection. SEM imaging of biological specimen usually necessitates a thin conductive coating to prevent negative charge accumulation from the impinging electrons. Such coatings, albeit only a few nm thick, can significantly alter and conceal fine details of biological nanostructures [2], which is noticeable on SEM images of virus particles [18],[23]. Since in the HIM, positive charge accumulates on insulating samples, a low-energy electron flood gun can be used for charge compensation, which irradiates the sample with a diffuse beam of electrons. This eliminates the need for a conductive coating, and allows a direct view on nanoscale structures [6],[24]. Here, we demonstrate the benefits of high-resolution HIM by imaging SARS-CoV-2 interacting with Vero E6 cells without any conductive coating. The presented images allow the identification of SARS-CoV-2 virus particles, their interaction with the cell membrane and a distinction between virus particles bound to from those lying on the cell surface.

Experimental

Vero E6 cells were cultivated in Dulbecco's modified Eagle's medium (Thermo Fisher Scientific) supplemented with 10% fetal bovine serum (Capricorn Scientific) in a 5% CO₂ atmosphere at 37 °C. SARS-CoV-2 (strain SARS-CoV-2 /München-1.2/2020/984, p.2) [25] was grown on Vero E6 cells and titrated as described [26]. Infection experiments were done under biosafety level 3 conditions with enhanced respiratory personal protection equipment.

For HIM, cells were seeded onto coverslips placed in 24 well plates. The coverslips were previously sputter coated with 30 nm of gold to improve charge neutralization during HIM imaging. After 24 h nearly confluent monolayers were infected with SARS-CoV-2 at a multiplicity of infection (MOI) of approximately 1 or mock infected using cell culture medium. Following an incubation period of 18 h in a cell culture incubator (37 °C) cells were washed with 0.1 M sodium cacodylate (NaCac) (pH 7.4) and fixed in 2% (v/v) glutaraldehyde, 2% (w/v) paraformaldehyde in NaCac-buffer at room temperature for 30 min and with fresh fixative overnight at 4 °C. The coverslips were subsequently washed and dehydrated in a graded series of ethanol (50%, 70%, 95%, 99,5% (2x)), transferred to water free acetone and critical point dried in carbon dioxide. HIM was performed with an Orion Plus (Carl Zeiss) at an acceleration voltage of about 36 kV and a working distance of 20 mm. The spot control was set to 6 to obtain a beam current of 0.2 to 0.4 pA. To avoid charging effects during secondary electron detection, an electron flood gun was used after each line scan, if not stated otherwise, with a flood energy of 540 eV, flood time of 10 μs and a focus of 107 V. It should be mentioned that the flood gun parameters have to be optimized for each magnification level. Before imaging, each sample was stored in the microscope's vacuum chamber at 3.3×10^{-7} mbar for at least 24 h to remove most volatile organic contaminants.

Results and Discussion

A comparison between a native and an infected Vero E6 cell at multiple magnification levels is shown in Fig. 1. Figure 1a shows a sequence of five HIM images of native Vero E6 cells (mock-infected). Fig 1b displays a sequence of HIM images of Vero E6 cells after they have been exposed to SARS-CoV-2 at a multiplicity of infection of approximately 1 (MOI 1). The surfaces of the infected cells are covered by a number of micrometer sized vesicles and segments of cell membranes, which is a first indication that apoptosis occurred during viral replication. Regularly shaped particles below 100 nm diameter on the cell membrane shown in Fig. 1b₄ and 1b₅ were only abundant on the cells of the MOI 1 sample and were therefore identified as SARS-CoV-2 virus particles. The cell membrane of the infected cell is covered with the virus particles, which are predominantly spherically shaped. Holes in the cell membrane, as illustrated in Fig. 1a₅ or Fig. 1b₄₋₅ (arrows), have previously been observed in uncoated mammalian cells and indicate lipid nanodomains or caveolea [6]. Figure 1c shows an evaluation of the virus particle size in five arbitrarily chosen regions on the MOI 1 sample resulting in an average diameter of the virus particles of (75.1 ± 12.8) nm, noting that this value has been obtained from viruses after fixation and critical point drying.

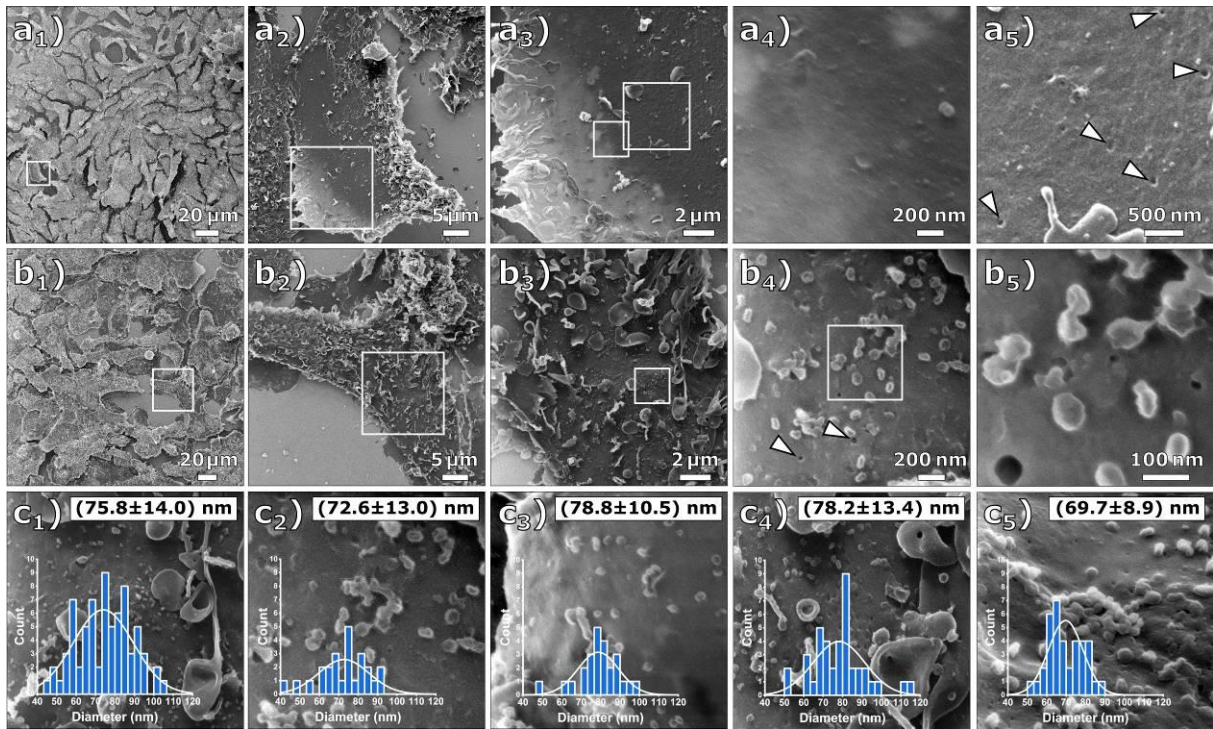


Fig. 1: Comparative HIM images of the mock-infected and at MOI 1 infected Vero E6 cells: a₁) – a₅) Mock-infected cell at different magnifications (FOV 200 μm, 45 μm, 15 μm, 1.7 μm, 3 μm) and b₁) – b₅) infected at MOI 1 cells at different magnifications (FOV 250 μm, 45 μm, 15 μm, 1.7 μm, 500 nm). The cell membrane is covered with the virus particles. c₁) – c₅) Virus particle diameter distributions determined. The inserted histograms show the respective image evaluation with normal distribution, mean value and standard deviation. The average diameter of all evaluated images is (75.1 ± 12.8) nm.

As the He⁺ ions can penetrate several hundred nanometers into the sample [27], the outer rim of the cells appears brighter because the ions pass through the cells and generate additional secondary electrons at the back of the cells and in the gold coated specimen slide [28]. The edges appear brightest where the cells bend upwards from the substrate. As shown in Fig. 2, the edge-resolution in two highly magnified images has been determined by plotting the corresponding grey scale values over the edges of two holes, resulting in values of 1.3 nm and 2.1 nm. The edge-resolution of the images is caused by an interplay between the size of the focused He⁺ beam and the widening of the beam within the sample material. The obtained values are typical for biological materials [6].

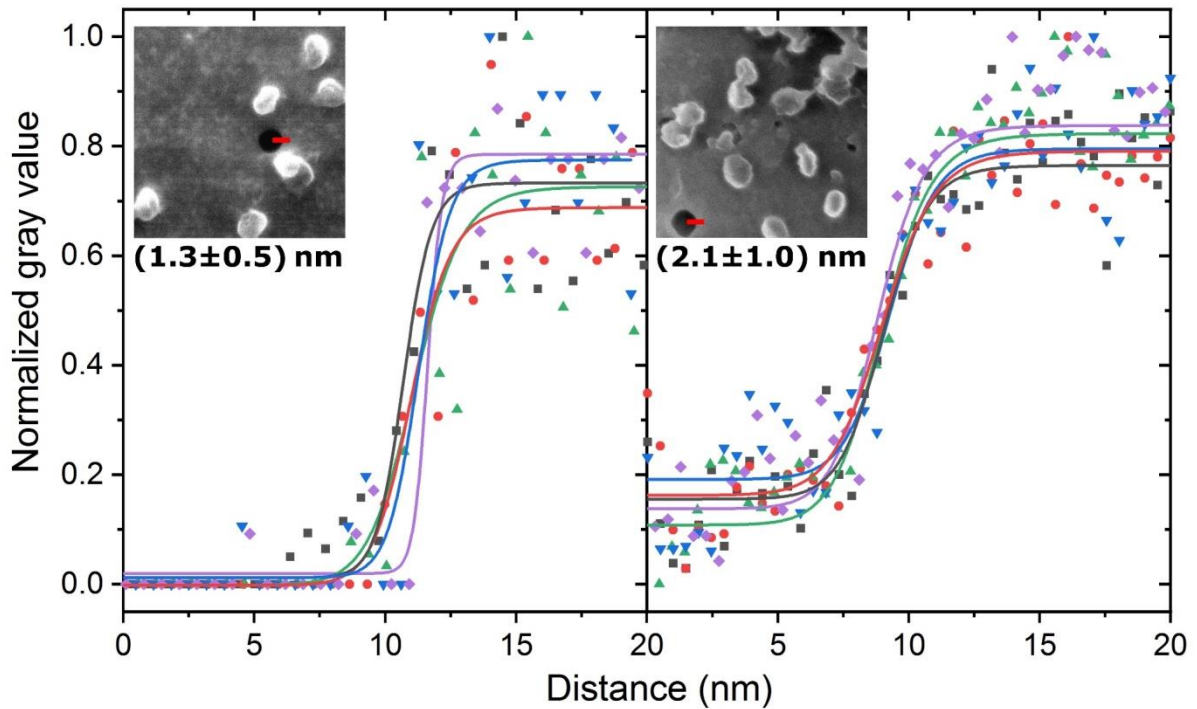


Fig. 2: Edge-resolution of two HIM images, averaged over 5 gray scale plots each that were fitted by logistic regression. The corresponding edges of holes in the cell membrane are shown in the inserted images (red lines); respective mean values and standard deviations of $d_{25\%-75\%}$ are given below.

An effect frequently occurring during HIM imaging with charge compensation can be observed in the sequence of HIM images shown in Fig. 3a₁₋₃, where a location on a MOI 1 infected Vero E6 sample was first imaged at a field of view (FOV) of 23 μm (Fig. 3a₁), followed by two higher magnification images with a FOV of 4.5 μm and a FOV of 1 μm (Fig. 3a₂). Fig. 3a₃ shows the same region as Fig. 3a₁, but the parts that were previously imaged at high magnification (FOV of 4.5 μm) with a dose of 1.4×10^{16} ions/cm² appear noticeably brighter. This is caused by the He⁺ beam induced carbonaceous deposits, which produce a thin conductive coating. In addition to improved conductivity of the specimen the deposited layer may contribute to the electron density of the surface, thus increasing secondary electron yield. This effect, commonly referred to as electron and/or ion beam induced deposition, is well known from charged particle microscopes. Residual gas in the HIM as well as the specimen

itself are considered the main contributor of hydrocarbons [29],[30]. This effect is therefore likely to be more pronounced when imaging biological samples in HIM.

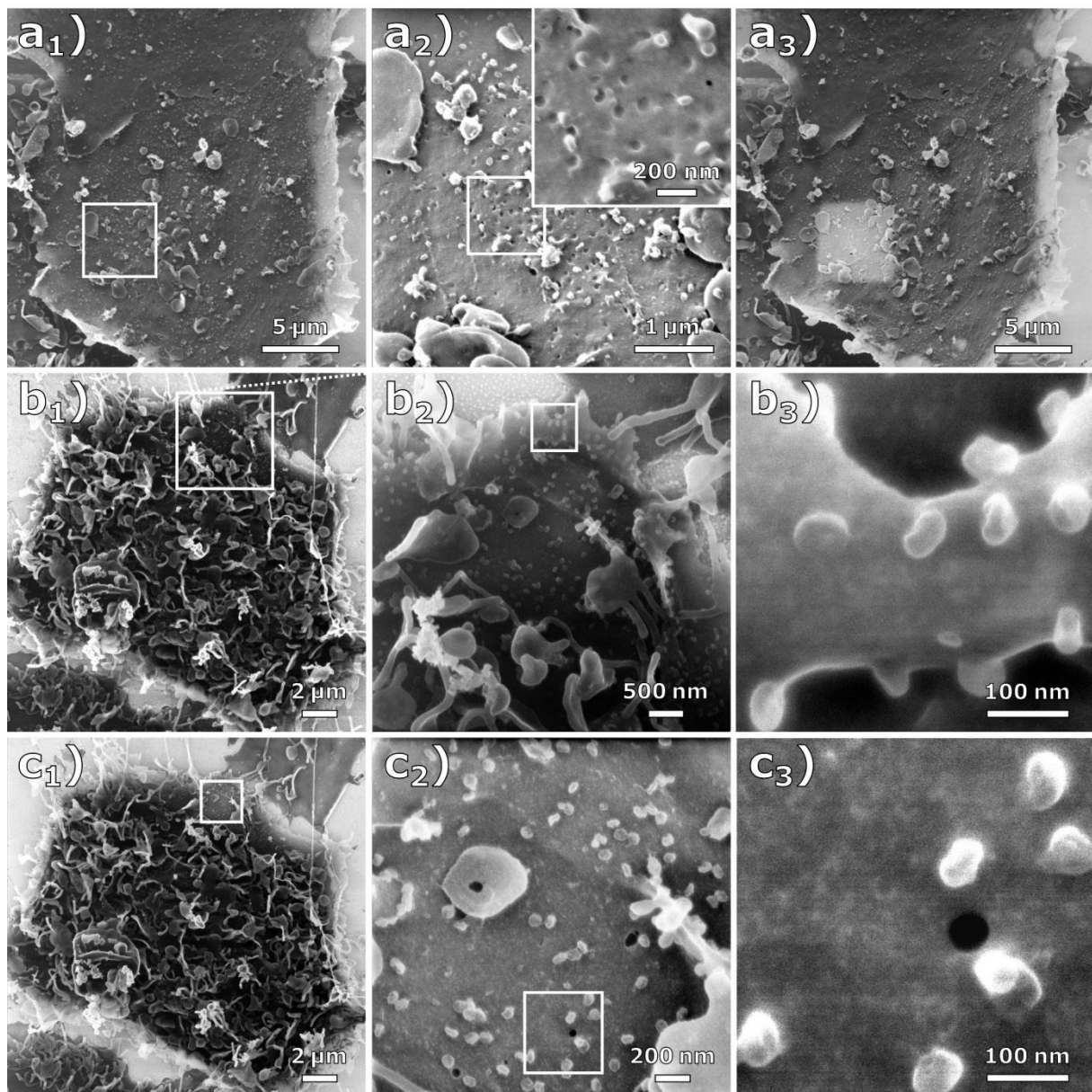


Fig. 3: Effect of carbon deposition during HIM imaging: a₁) HIM image (FOV 20 μm) of a cell infected at MOI 1 with charge compensation. a₂) HIM images at high magnification (FOV 4.5 μm and 1 μm) with charge compensation. a₃) The same image section as a₁) after imaging the regions in a₂. Due to increased conductivity, this region appears significantly brighter than the rest of the image. b₁) – b₃) HIM images of a cell infected at MOI 1 at different magnifications (FOV 20 μm, 5 μm, 450 nm) with charge compensation; c₁) – c₃) HIM images of the same cell (FOV 20 μm, 2 μm, 450 nm) after imaging the magnified sections in b), c₁) – c₂) with and c₃) without charge compensation.

Fig. 3b₁-b₃ shows an infected Vero E6 cell at different magnification levels. Fig. 3b₃ depicts the highest magnification (FOV 450 nm) of the cell seen in Fig. 3b₁, showing the virus particles on top of the cell membrane in a side view. Note that after the zoom-out in Fig. 3c₁, the previously imaged regions appear again brighter. After imaging Fig. 3c₂ with a dose of 1.9×10^{17} ions/cm², the flood gun was turned off, which allowed imaging of Fig. 3c₃ without any external charge compensation. From the quality of this image, it can be inferred that the deposited carbon layer rendered the sample sufficiently conductive. However, small structures are still visible on the membrane surface, which may originate from surface topography or material contrast. The deposited carbon is presumably thinner than typical conductive metal or carbon coatings for SEM imaging, and it does not show any surface masking and clustering as seen on the gold substrate in the upper left of Fig. 3b₂. The energy of the incident hydrocarbons is much lower compared to the energy of sputter deposited metals, however, it is possible that this unintended but useful carbon layer can be avoided by HIM operation in ultra-high vacuum [31],[32],[33].

The cell structures shown in the HIM images of Fig. 4a are sharply resolved over tens of μm , which demonstrates the high depth of field of HIM compared to SEM [34]. In image 4a₃ at the surface of the cell a cluster of virus particles seems to be bound to the cell membrane (arrow). We suggest that this resembles the particle clustering by host defense protein BST-2 as it was observed for human coronavirus229E and quantified in HeLa cells by Wang et al. [35]. However, the metal coating applied by Wang et al. is clearly visible at high resolution in the SEM images as a rough layer on the cell membrane and hiding the true topography [24],[24],[36]. In contrast, the HIM images presented here not only allow for the quantification of particles and clusters, but also enable an unveiled view on the interaction of virus particles with the cell membrane. The presented particle cluster seems to have a coalesced appearance,

which might be caused by the agglutinating BST-2 mediated virus-virus and virus-membrane interaction [37],[38]. Furthermore, elongated membrane structures between the virus particles and the cell membrane became visible (arrowheads). Fig. 4b shows another cell on the MOI 1 sample at different magnification levels. In the highest magnification shown in Fig. 4b₃ (FOV 850 nm), the ultrastructure of these tubular structures is depicted (arrowheads). Their ridge-like structures give these tubular connections the appearance of a tensed freely suspended membrane linking the virus particles to the cell membrane. We assume that this resembles the tubulating cell membrane, which is stabilized by BST-2 to prevent viral scission. This alternative BST-2 interaction was already described for HIV infected cells via immuno-TEM [39], but has not yet been observed for SARS-CoV-2. Aside from this observation the HIM images allow the distinction between these viruses bound to the membrane and virus particles lying on top of the membrane (Fig. 4b, arrows). Compared to a SEM study, in which all visible virus particles on a cell membrane were quantified [38], HIM images could provide additional information about bound and unbound particles, resulting in more accurate data by counting only the bound particles. The presented images demonstrate, that the HIM is well suited for the imaging of virus-membrane and virus-virus interactions, e.g. when the virus particles are bound to the cell membrane or/and have a coalesced appearance.

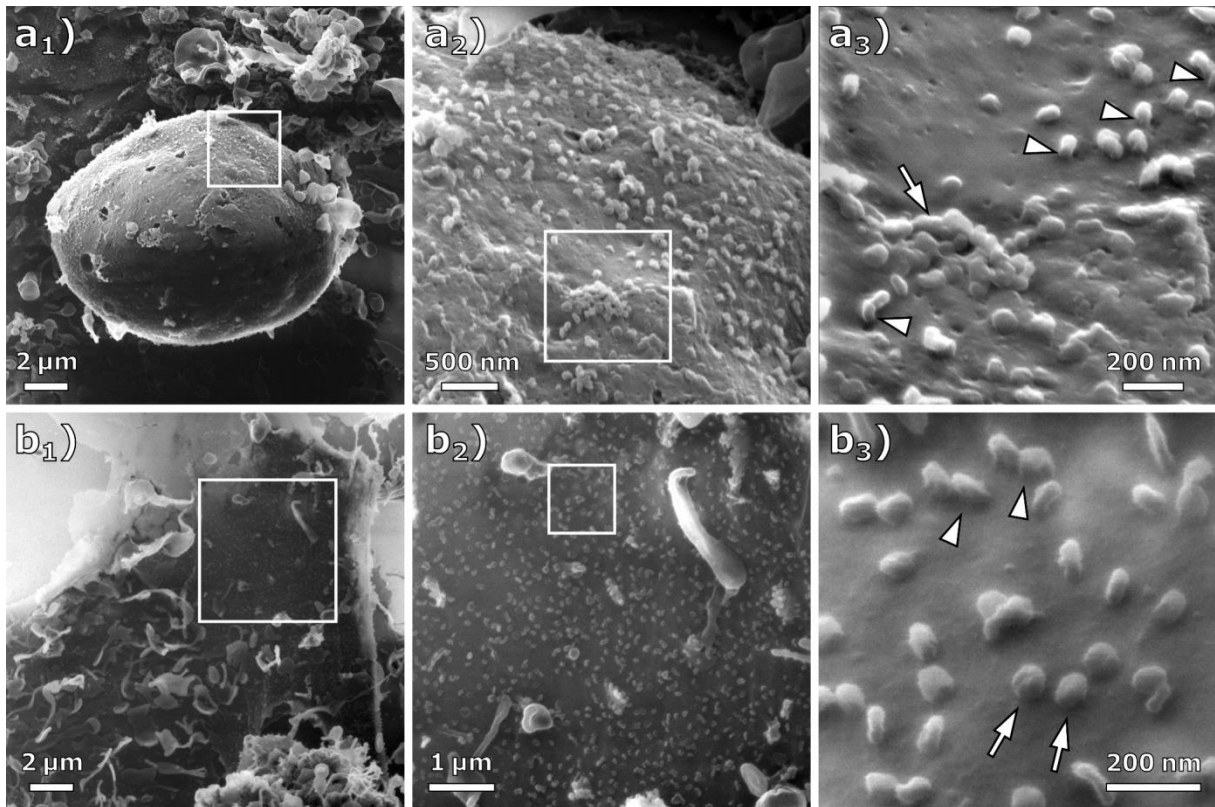


Fig. 4: HIM images of cells infected at MOI 1 imaged with charge compensation. a₁) – a₃) Different magnifications of an infected cell (FOV 17 μm, 3.5 μm, 1.3 μm). At high magnification a₃) clusters of virus particles (arrow) and tubular membrane structures (arrowheads) between the virus particle and the cell membrane become visible. b₁) – b₃) Different magnifications of an infected cell (FOV 18 μm, 6 μm, 850 nm). At even higher magnification the ultrastructure of this tubular structure becomes visible. Ridge like structure, resembling taunted cell membrane, can be observed between the virus particle and the cell surface (arrowheads). Unbound viruses (arrows), just lying on top of the cell, can be easily distinguished from these bound viral particles.

It is known that the spike glycoproteins can be visualized by TEM. As the HIM images depicted the virus particles without conductive coating, it is an interesting question, whether or not the spike glycoproteins could in principle be resolved in HIM images. Inspecting our highest magnification images, Figs 3b₃ and 3c₃, we do not see unequivocal evidence of structures indicating the spike glycoproteins, however, it is

conceivable that a dedicated sample preparation could preserve their structure for imaging in HIM.

Conclusion

In this study, HIM images of Vero E6 cells without infection and infected with SARS-CoV-2 are presented. On infected cells the ultrastructure of the cell-virus interaction, as well as among virus particles, could thus be shown. The absence of a previously applied conductive coating allowed the distinction between virus particles bound to the cell membrane and virus particles lying on top of the cell membrane. The images unveil the three-dimensional appearance of SARS-COV-2 and the surface of Vero E6 cells at MOI 1 with an edge-resolution of up to 1.3 nm. Additionally, it has been shown, that ion-induced deposition renders the sample surface sufficiently conductive to be imaged without charge compensation. The presented images demonstrate the potential of the HIM in bioimaging, especially for the imaging of interactions between viruses and their host organisms. HIM thus represents a versatile complement to conventional methods in the life sciences.

Acknowledgement

F.W. is funded by the LOEWE Centre for Novel Drug Targets against Poverty-Related and Neglected Tropical Infectious Diseases (DRUID), which is part of the excellence initiative of the Hessen State Ministry of Higher Education, Research and the Arts (HMWK), the RAPID consortium of the Federal Ministry of Education and Research (BMBF, grant number 01KI1723E), and the European Union's Horizon 2020 research and innovation program under grant agreement No 101003666 (OPENCORONA). This

Work was further conducted within the framework of the COST Action CM19140 (FIT4NANO). The authors thank André Beyer and Daniel Emmrich for valuable discussion.

References

- [1] Hlawacek, G.; Götzhäuser, A. *Helium Ion Microscopy*, **2016**, 395-414.
- [2] Vanden Berg-Foels, W. S.; Scipioni, L.; Huynh, C.; Wen, X. *Journal of microscopy*, **2012**, 246(2), 168-176.
- [3] Bazou, D.; Behan, G.; Reid, C.; Boland, J. J.; Zhang, H. Z. *Journal of microscopy*, **2011**, 242(3), 290-294.
- [4] Chen, X.; Udalagama, C. N.; Chen, C. B.; Bettiol, A. A.; Pickard, D. S.; Venkatesan, T.; Watt, F. *Biophysical journal*, **2011**, 101(7), 1788-1793.
- [5] Rice, W. L.; Van Hoek, A. N.; Păunescu, T. G.; Huynh, C.; Goetze, B.; Singh, B.; Scipioni, L.; Stern, L. A.; Brown, D. *PloS one*, **2013**, 8(3), e57051.
- [6] Schürmann, M.; Frese, N.; Beyer, A.; Heimann, P.; Widera, D.; Mönkemöller, V.; Huser, T.; Kaltschmidt, B.; Kaltschmidt, C.; Götzhäuser, A. *Small*, **2015**, 11(43), 5781-5789.
- [7] Greiner, J. F.; Hauser, S.; Widera, D.; Müller, J.; Qunneis F.; Zander, C.; Martin, I.; Mallah, J.; Schuetzmann, D.; Prante, C.; Schwarze, H.; Prohaska, W.; Beyer, A.; Rott, K.; Hütten, A.; Götzhäuser, A.; Sudhoff, H.; Kaltschmidt, C.; Kaltschmidt, B. *European Cells and Materials*, **2011**, 22, 403-419.
- [8] Leppänen, M.; Sundberg, L. R.; Laanto, E.; de Freitas Almeida, G. M.; Papponen, P.; Maasilta, I. J. *Advanced Biosystems*, **2017**, 1(8), 1700070.
- [9] Said, N.; Chatzinotas, A.; Schmidt, M. *Advanced Biosystems*, **2019**, 3(1), 1800250.

- [10] Chen, S. C.; Musat, N.; Lechtenfeld, O. J.; Paschke, H.; Schmidt, M.; Said, N.; Popp, D.; Calabrese, F.; Stryhanyuk, H.; Jaekel, U.; Zhu, Y. G.; Joye, S. B.; Richnow, H. H.; Widdel, F.; Musat, F. *Nature*, **2019**, 568(7750), 108-111.
- [11] Corman, V. M.; Lienau, J.; Witzentz, M. *Der Internist*, **2019**, 60(11), 1136-1145.
- [12] Wu, F.; Zhao, S.; Yu, B.; Chen, Y. M.; Wang, W.; Song, Z. G.; Hu, Y.; Tao, Z. W.; Tian, J. H.; Pei, Y. Y.; Yuan, M. L.; Zhang, Y. L.; Dai, F. H.; Liu, Y.; Wang, Q. M.; Zheng, J. J.; Xu, L.; Holmes, E. C.; Yuan, M. L. *Nature*, **2020**, 579(7798), 265-269.
- [13] Coronavirus COVID-19 Dashboard, Johns Hopkins University. <https://gisanddata.maps.arcgis.com/apps/opsdashboard/index.html#/bda7594740fd40299423467b48e9ecf6> (accessed Dec 01, **2020**)
- [14] Takayama, K. *Trends in Pharmacological Sciences*, **2020**, 41(8), 513-517.
- [15] Zhu, N.; Zhang, D.; Wang, W.; Li, X.; Yang, B.; Song, J.; Zhao, X.; Huang, B.; Shi, W.; Lu, R.; Niu, P.; Zhan, F.; Ma, X.; Wang, X.; Xu, W.; Wu, G.; Gao, G. F.; Tan, W. *New England Journal of Medicine*, **2020**, 382, 727-733.
- [16] Algarroba, G. N.; Rekawek, P.; Vahanian, S. A.; Khullar, P.; Palaia, T.; Peltier, M. R.; Cavez, M. R.; Vintzileos, A. M. *American Journal of Obstetrics & Gynecology*, **2020**, 223(2), 275-278.
- [17] Harcourt, J.; Tamin, A.; Lu, X.; Kamili, S.; Sakthivel, S. K.; Murray, J.; Queen, K.; Tao, Y.; Paden, C. R.; Zhang, J.; Li, Y.; Uehara, A.; Wang, H.; Goldsmith, C.; Bullock, H. A.; Wang, L.; Whitaker, B.; Lynch, B.; Gautam, R.; Schindewolf, C.; Lokugamage, K. G.; Scharon, D.; Plante, J. A.; Mirchandani, D.; Widen, S. G.; Narayanan, K.; Makino, S.; Ksiazek, T. G.; Plante, K. S.; Weaver, S. C.; Lindstorm, S.; Tong, S.; Menachery, V. D.; Thornburg, N. J. *Emerging infectious diseases*, **2020**, 26(6), 1266.

- [18] Bouhaddou, M.; Memon, D.; Meyer, B.; White, K. M.; Rezelj, V. V.; Marrero, M. C.; Polacco, B. J.; Melnyk, J. E.; Ulferts, S.; Kaake, R. M.; Batra, J.; Richards, A. L.; Stevenson, E.; Gordon, D. E.; Rojc, A.; Obernier, K.; Fabius, J. M.; Soucheray, M.; Miorin, L.; Moreno, E.; Koh, C.; Tran, Q. D.; Hardy, A.; Robinot, R.; Vallet, T.; Nilsson-Payant, B. E.; Hernandez-Armenta, C.; Dunham, A.; Weigang, S.; Knerr, J.; Modak, M.; Quintero, D.; Zhou, Y.; Dugourd, A.; Valdeolivas, A.; Patil, T.; Li, Q.; Hüttenhain, R.; Cakir, M.; Muralidharan, M.; Kim, M.; Jang, G.; Tutuncuoglu, B.; Hiatt, J.; Guo, J. Z.; Xu, J.; Bouhaddou, S.; Mathy, C. J. P.; Gaulton, A.; Manners, E. J.; Félix, E.; Shi, Y.; Goff, M.; Lim, J. K.; McBride, T.; O'Neal, M. C.; Cai, Y.; Chang, J. C. J.; Broadhurst, D. J.; Klippsten, S.; De wit, E.; Leach, A. R.; Kortemme, T.; Shoichet, B.; Ott, M.; Saez-Rodriguez, J.; tenOever, B. R.; Mullins, R. D.; Fischer, E. R.; Kochs, G.; Grosse, R.; García-Sastre, A.; Vignuzzi, M.; Johnson, J. R.; Shokat, K. M.; Swaney, D. L.; Beltrao, P.; Krogan, N. J. *Cell*, **2020**, Volume 182, Issue 3, 685-712
- [19] Prasad, S.; Potdar, V.; Cherian, S.; Abraham, P.; Basu, A.; Team, I. N. N. *The Indian journal of medical research*, **2020**, 151(2-3), 241.
- [20] Wolff, G.; Limpens, R. W.; Zevenhoven-Dobbe, J. C.; Laugks, U.; Zheng, S.; de Jong; A. W. M.; Koning, R. I.; Agard, D. A.; Grünewald, K.; Koster, A. J.; Snijder, E. J.; Bárcena, M. *Science*, **2020**. DOI: 10.1126/science.abd3629
- [21] Ward, B. W.; Notte, J. A.; Economou, N. P. *Journal of Vacuum Science & Technology B*, **2006**, 24(6), 2871-2874.
- [22] Hlawacek, G.; Veligura, V.; van Gastel, R.; Poelsema, B. *Journal of Vacuum Science & Technology B*, **2014**, 32(2), 020801.
- [23] "New Images of Novel Coronavirus SARS-CoV-2 Now Available", NIAID Media Team, Feb 17, 2020, USA. <https://www.niaid.nih.gov/news-events/novel-coronavirus-sarscov2-images> (accessed Dec 01, **2020**)

- [24] Joens, M. S.; Huynh, C.; Kasuboski, J. M.; Ferranti, D.; Sigal, Y. J.; Zeitvogel, F.; Obst, M.; Burkhardt, C. J.; Curran, K. P.; Chalasani, S. H.; Stern, L. A.; Goetze, B.; Fitzpatrick, J. A. J. *Scientific reports*, **2013**, 3, 3514.
- [25] Rothe, C.; Schunk, M.; Sothmann, P.; Bretzel, G.; Froeschl, G.; Wallrauch, C.; Zimmer, T.; Thiel, V.; Janke, C.; Guggemos, W.; Seilmaier, M.; Drosten, C.; Vollmar, P.; Zwirgmaier, K.; Zange, S.; Wölfel, R.; Hoelscher, M. *New England Journal of Medicine*, **2020**, 382(10), 970-971.
- [26] Felgenhauer, U.; Schoen, A.; Gad, H. H.; Hartmann, R.; Schaubmar, A. R.; Failing, K.; Drosten, C.; Weber, F. *Journal of Biological Chemistry*, **2020**, 295(41), 13958-13964.
- [27] Cohen-Tanugi, D.; Yao, N. *Journal of Applied Physics*, **2008**, 104(6), 063504.
- [28] Bell, D. C. *Microscopy and Microanalysis*, **2009**, 15(2), 147-153.
- [29] Isaacson, M. *Ultramicroscopy*, **1979**, 4(2), 193-199.
- [30] Hren, J. J. *Ultramicroscopy*, 3(4), **1978**, 375-380.
- [31] van Gastel, R.; Barriss, L.; Sanford, C.; Hlawacek, G.; Scipioni, L.; Merkle, A. P.; Voci, D.; Fenner, C.; Poelsema, B. *Microscopy and microanalysis*, **2011**, 17(S2), 928.
- [32] Hlawacek, G.; Veligura, V.; Lorbek, S.; Mocking, T. F.; George, A.; van Gastel, R.; Zandvliet, H. J. W.; Poelsema, B. *Beilstein journal of nanotechnology*, **2012**, 3(1), 507-512.
- [33] Veligura, V.; Hlawacek, G.; van Gastel, R.; Zandvliet, H. J.; Poelsema, B. *Beilstein journal of nanotechnology*, **2012**, 3(1), 501-506.
- [34] Wirtz, T.; De Castro, O.; Audinot, J. N.; Philipp, P. *Annual Review of Analytical Chemistry*, **2019**, 12, 523-543.
- [35] Wang, S. M.; Huang, K. J.; Wang, C. T. *Virology*, **2014**, 449, 287-296.

- [36] Caldas, L. A.; Carneiro, F. A.; Higa, L. M.; Monteiro, F. L.; da Silva, G. P.; da Costa, L. J.; Durigon, E. L.; Tanuri, A.; de Souza, W. *bioRxiv*, **2020**.
- [37] Mahauad-Fernandez, W. D.; Okeoma, C. M. *Immunity, inflammation and disease*, **2016**, 4(1), 4-23.
- [38] Berry, K. N.; Kober, D. L.; Su, A.; Brett, T. J. *BioEssays*, **2018**, 40(10), 1800086.
- [39] Hammonds, J.; Wang, J. J.; Yi, H.; Spearman, P. *PLoS Pathog*, **2010**, 6(2), e1000749.